*Jordan Journal of Civil Engineering,* Volume **16**, No. **4**, **2022**

# A Finite Element Method for Modeling Edge Effects in Composite Laminates with Different Ply Orientations

***Karim S. Numayr [1], Ayman N. Ababneh [2] and Hashem K. Almashaqbeh [1]****

[1] Department of Civil Engineering, Isra University, Amman, Jordan.
[2] Department of Civil Engineering, Jordan University of Science and Technology, Irbid, Jordan.
***** Corresponding Author. E-Mail: H.almashaqbeh@iu.edu.jo

## ABSTRACT

A finite element (FE) method is used for modeling edge effects in composite laminates with different ply orientations. Two types of three-dimensional isoperimetric FE methods have been used. One in the interior region has standard linear shape functions, while the other in the exterior region has special shape functions for which an exponential variation is derived using the perturbation technique. The exponential shape functions are introduced to an originally written FE program which uses special mesh generation and numerical integration, as well as other subroutines. The proposed FE solution is found to be in good agreement with the solutions available in the literature.

**KEYWORDS:** Finite-element modeling, Perturbation technique, Laminated composites, Edge effect, Delamination.

## INTRODUCTION

Composite materials have received increasing attention due to their wide engineering applications, especially in the aircraft and spacecraft industries, because of their high strength-to-weight ratio and stuffiness-to-weight ratio (Cao et al., 2019; Dölling et al., 2020; Kumar et al.,2020; Lecomte-Grosbras et al., 2014; Shen et al., 2020). Many properties can be improved by forming a composite material, including strength, stiffness, corrosion and wear resistance, weight, fatigue life, temperature-dependent behavior, thermal insulation, thermal conductivity and acoustical insulation (Yang et al., 2011). The idea of composite materials is not new or recent, since nature is full of composite material structures, such as wood, bone and coconut palm leaf. Beside these naturally occurring composites, many other engineering materials are composites in a very general way, such as carbon black in rubber, Portland cement or asphalt mixed with sand and glass fibers in resin. One can safely mark the origin of a distinct discipline of composite materials since the beginning of the 1960s (Cater et al., 2018; Dölling et al., 2020). Composite materials can be classified into three major categories, including fiber composites, particulate composites and laminated composites (Pereira & Martins, 2014). Lamination is used to combine the best aspects of the constituents' layers in order to achieve a more useful material. A potential problem in the construction of laminates is the introduction of shearing stress between layers. The shearing stress arises due to the tendency of each layer to deform independently of its neighbors, because all may have different properties. Such shearing stresses are largest at the edges of the laminate and may cause delamination there. Therefore, the distribution of stress near the free edges should be determined very precisely due to its significant impact on delamination in layered laminates.

The free-edge effect in an asymmetrically laminated composite plate subjected to a uniform uniaxial extension has been investigated by utilizing both experimental and analytical approaches. The experimental results have verified the presence of large displacement gradients and a large, but finite, strain concentration at the free-edge region (Cao et al., 2019; Herakovich et al., 1985;

Received on 28/10/2021.
Accepted for Publication on 3/6/2022.

Lecomte-Grosbras et al., 2014; Lorriot et al., 2013; Oplinger et al., 1974; Romera et al., 2013). It has also been experimentally verified that strain concentrations are limited to the narrow boundary-layer region along the free edges. Delamination has been experimentally observed (Herakovich et al., 1985; Oplinger et al., 1974). Numerous analytical procedures have been developed to calculate interlaminar stresses. These procedures utilized a variety of techniques, including finite difference, boundary-layer theory, perturbation method, series solution, displacement finite element, hybrid finite element, a mixture of strength of materials, classical lamination theory and elasticity. Pipes and Pagano (1970) published the first complete, three-dimensional analysis of interlaminar stress in laminated composites subjected to axial loading, based on a linear elastic generalized plane strain formulation using the finite difference method. Their results demonstrated the existence of all three components of interlaminar stress in a boundary-layer region along the free edges of the plate. Since a coarse grid is used to reduce the computing storage and computing time, their results are not detailed enough to allow accurate evaluation of stresses near the free-edge region. Pagano (1978) introduced a new theory based on an extension of Reissner's variation theorem to define the stress filed within an arbitrary composite laminate. Although his proposed solution faces some difficulties to define the stress fields in laminates consisting of many layers, the solution provides good results for composite laminates with few layers. In 2018, a classic finite difference system comparable to that proposed by Pipes has been implemented by Solis et al. (2018). They studied the dependence out-of-plane stresses on interlaminar stress and fiber orientation by analyzing symmetric laminates with varying stacking sequences. The results indicated that the variation in interlaminar stresses at the free edge, considering the fiber orientation, was different in the laminate lay-ups. Nonetheless, fiber orientation and its value at which the maximum shear stress appears were found to be similar in all cases. Hsu and Herakovich (1977) used a zero-order perturbation approximation in terms of displacement functions along with a limiting free-body approach in order to establish a solution to the governing system of partial differential equations. This solution depends on the geometric thickness-to-width-ratio. The solution predicts a continuous distribution of interlaminar stresses with maximum values at the free-edge boundary region. Wang and Dickson (1978) used Legendre polynomials to represent interlaminar stresses and displacements for each layer. The extended Galerkin method was used to satisfy the equilibrium equations for each layer of continuity at the interfaces of the layers and satisfaction of stress boundary conditions at the exterior planes led to the final solution. Their predicted results for normal stress were high at the free-edge region. Kassapoglou and Lagace (1987) presented a closed-form solution for the problem of interlaminar stresses at a straight free-edge in a composite laminate for two special cases; angle-ply and cross-ply laminates. The solution was derived using the force-balance method and the principle of minimum complementary energy. The obtained results agreed very well with the results available in the literature for the same problem, except for the cross-ply laminates. Herakovich (1989) discussed the relationship between the morphology of a composite laminate and the resulting free-edge effects in the shape of interlaminar stress concentrations which may lead to delamination failure. Cross-ply, angle-ply and quasi-isotropic laminates were discussed in detail. It is shown that the local mismatch in elastic properties of adjacent layers and the global stacking sequence of a laminate both have a significant influence on interlaminar stresses and delamination failures. Over the past few decades, several researchers studied free-edge stresses using the finite element (FE) method (Bar-Yoseph & Avrashi, 1986; Cao et al., 2019; Cater et al., 2018; Chorng-Fuh & Horng-Shian, 1993; Dölling et al., 2020; Espadas-Escalante et al., 2018; Islam & Prabhakar, 2017; Nguyen & Caron, 2009, 2006; Numayr, 1987; Wang & Crossman, 1977). Wang and Crossman (1977) used a triangular finite element in the investigation of the stress field closest to the ply interfaces and the free-edge regions of a symmetrically laminated plate subjected to constant axial strain. Their formulation is based on constant strain within each element. Bar-Yoseph and Avrashi (1986) used a modified mixed-hybrid FE in the solution of the free-edge boundary layer problem. They carried out a three-dimensional stress analysis. Numayr (1987) developed an FE model based on an approximate analytical solution. Plane-strain formulation was used. The results obtained are limited to cross-ply laminates. Chorng-Fuh and Horng-Shian (1993) presented a mixed FE model. In their model, three transverse stresses are included as a nodal degree of freedom besides

displacements in the three Cartesian coordinate directions. With such a formulation, the stress continuity condition at the interlayers and the free transverse stress conditions on boundaries can then be satisfied naturally in the analysis of interlaminar stress problems. More recently, Cater et al. (2018) developed atwo-scale FE model in order to study the effect of interlaminar microstructure at the free-edge of a laminate. The results confirmed that the matrix stress at the free-edge is highly dependent on the interlaminar microstructure. For instance, the more matrix content, the more matrix stress during thermal cool down and the less matrix stress under tensile loading. Islam and Prabhakar (2017) analyzed the stresses at the free edges in composite laminates subjected to uniform axial and/or thermal load. An FE model based on a quasi-2D plane strain formulation was developed to predict the interlaminar stresses in multi-directional laminates. They found that by using the quasi-2D model, the computational time needed to estimate the interlaminar stresses was 30 times lower than the 3D analysis of the same laminate. Mohammadi and Salimi-Majd (2014) studied the modes of failure in cross-ply and angle-ply laminates using FE approach. In their study, the cohesive-zone model has been implemented in order to develop the interface element. The results showed that in angle-ply laminates, delamination in the shear mode is dominant. Moreover, in cross-ply laminates, the damage behavior is found to be highly dependent on the stacking sequence of the laminates. A multi-particle FE approach has been implemented by Nguyen and Caron (2009) to analyze the free-edge stresses of composite laminates. Their model has been developed based on the eight-node layer-wise finite element. The finite element results demonstrated that the model is able to provide accurate results and can be used as an operational tool to estimate the interlaminar stresses of composite laminates subjected to mechanical and thermal loading.

The present study focuses on developing a new FE approach to investigate the free-edge effects in composite laminates with different ply orientations. Since most of the other methods are facing some challenges, including defining the displacement and stress fields near the free-edge regions and determination of the narrow boundary width, the present method is proposed to overcome these problems. A novel 3-D FE model is developed based on an approximate analytical solution. The shape functions for the free-edge boundary region are derived using the perturbation technique, while the Galerkin approximation is employed to make theses shape functions satisfy the governing system of partial differential equations. As a result, the proposed FE model is able to obtain accurate results using a small number of elements. An original, detailed FE computer program has been written to solve the edge-effect problem of laminated composites. It includes all required subroutines needed; mesh generation, node and element numbering, matrix operations, element stiffness matrices, numerical integration, assemblage, partitioning, solution of a system of linear equations, … etc. It has been used to analyze composite laminates with different laminate geometries, different laminate sequences and different laminate materials subjected to uniaxial stretching. Furthermore, the results obtained from the present solution are compared with the results of other available solutions including finite difference (Pagano, 1978; Pipes & Pagano, 1970), finite element (Numayr, 1987; Wang & Crossman, 1977), perturbation technique (Hsu & Herakovich, 1977) and analytical solution based on Legendre polynomials and extended Galerkin method (Wang & Dickson, 1978).

**Problem Formulation**

Consider the balanced symmetrical composite laminated plate shown in Figure 1, subjected to a uniform axial extension $\epsilon_0$ in the $x$ direction. The order of the dimensions is $L_1>L_2>>L_3$ and the thickness-to-width ratio ($L_3/L_2$) is small. The laminates are homogenous and orthotropic with one of the orthotropic axes coinciding with the $z$-axis. The laminates are of thicknesses ($h_1/ h_2/ h_3/\ldots/ h_m$) and are oriented at angles ($\theta_1/\theta_2/\theta_3/,\ldots/\theta_m$) , with respect to the $x$-axiis.

The generalized Hooke's law relating stresses to strains is:

$$\begin{Bmatrix}\sigma_x\\ \sigma_y\\ \sigma_z\\ \tau_{yz}\\ \tau_{zx}\\ \tau_{xy}\end{Bmatrix}=\begin{bmatrix}E_{11} & E_{12} & E_{13} & 0 & 0 & E_{16}\\ E_{12} & E_{22} & E_{23} & 0 & 0 & E_{26}\\ E_{13} & E_{23} & E_{33} & 0 & 0 & E_{36}\\ 0 & 0 & 0 & E_{44} & E_{45} & 0\\ 0 & 0 & 0 & E_{45} & E_{55} & 0\\ E_{16} & E_{26} & E_{36} & 0 & 0 & E_{66}\end{bmatrix}\begin{Bmatrix}\epsilon_x\\ \epsilon_y\\ \epsilon_z\\ \gamma_{yz}\\ \gamma_{zx}\\ \gamma_{xy}\end{Bmatrix} \quad (1)$$

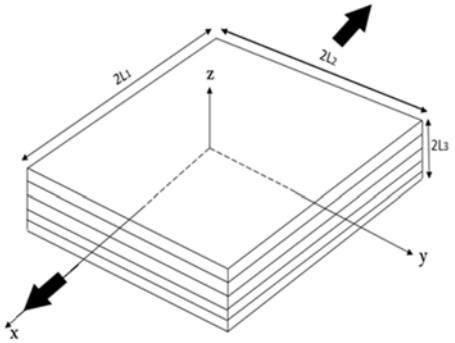


(a)

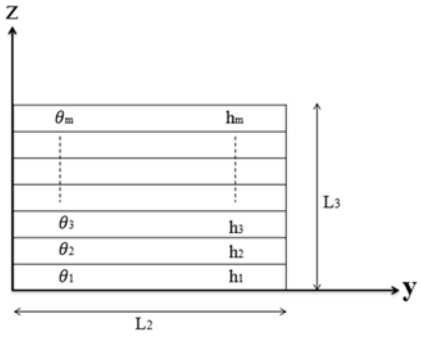


(b)

**Figure (1): (a) 2-m composite laminate subjected to a uniform uniaxial extension $\epsilon_0$. (b) *y-z* plane shows laminates with different angle orientations and thicknesses**

where, $\{\sigma\}$ is the stress vector, $\{\epsilon\}$ is the strain vector and $[E] =$ is the elasticity matrix. When one of the orthotropic axes of the laminate coincides with the *z*-axis, constitutive equations of an orthotropic material with respect to the coordinate axes *x,y,z*; only 13 elastic independent constants are necessary to define the three-dimensional constitutive equations. Laminates are considered long and only loaded at their ends $x = \pm L_1$. Saint Venant principle can be invoked, resulting in the conclusion that the stresses in regions far away from the ends are independent of *x* and $\frac{\partial \sigma_x}{\partial x} = \frac{\partial \tau_{xz}}{\partial x} = \frac{\partial \tau_{xy}}{\partial x} = 0$. Thus, the equilibrium equations in such regions are:

$$\begin{aligned} \frac{\partial \tau_{xy}}{\partial y} + \frac{\partial \tau_{zx}}{\partial z} &= 0 \\ \frac{\partial \sigma_y}{\partial y} + \frac{\partial \tau_{yz}}{\partial z} &= 0 \\ \frac{\partial \tau_{yz}}{\partial y} + \frac{\partial\, \sigma_z}{\partial z} &= 0 \end{aligned} \quad \text{... (2)}$$

Using strain-displacement and stress-strain relations, as well as applying symmetrical and anti-symmetrical conditions, the following system of simultaneous partial differential equations is obtained for each layer:

$$\begin{aligned} &\{E_{66}U_{,yy} + E_{55}U_{,zz} + E_{26}V_{,yy} + E_{45}V_{,zz} + (E_{36} + E_{45})W_{,yz}\}^{(k)} = 0 \\ &\{E_{26}U_{,yy} + E_{45}U_{,zz} + E_{22}V_{,yy} + E_{44}V_{,zz} + (E_{23} + E_{44})W_{,yz}\}^{(k)} = 0 \\ &\{(E_{45} + E_{36})U_{,yz} + (E_{44} + E_{23})V_{,yz} + E_{44}W_{,yy} + E_{33}W_{,zz}\}^{(k)} = 0 \end{aligned} \quad \text{... (3)}$$

Boundary condition equations at $y = \pm L_2$ are:

$$\begin{aligned} &\{E_{12}\, \epsilon_0 + E_{22}V_{,y}(\pm L_{2,}z) + E_{23}W_{,z}(\pm L_{2,}z) + E_{26}U_{,y}(\pm L_{2,}z)\}^{(k)} = 0 \\ &\{E_{16}\, \epsilon_0 + E_{26}V_{,y}(\pm L_{2,}z) + E_{66}U_{,y}(\pm L_{2,}z)\}^{(k)} = 0 \\ &\{E_{44}V_{,x}(\pm L_{2,}z) + E_{44}W_{,y}(\pm L_{2,}z) + E_{45}U_{,z}(\pm L_{2,}z)\}^{(k)} = 0 \end{aligned} \quad \text{... (4)}$$

and boundary condition equations at $z = \pm L_3$ are:

$$\begin{aligned} &\{E_{13}\, \epsilon_0 + E_{23}V_{,y}(y, \pm L_3) + E_{33}W_{,z}(y, \pm L_3 + E_{36}U_{,y}(y, \pm L_3)\}^{(m)} = 0 \\ &\{E_{44}V_{,z}(y, \pm L_3) + E_{44}W_{,y}(y, \pm L_3) + E_{45}U_{,z}(y, \pm L_3)\}^{(m)} = 0 \\ &\{E_{45}V_{,z}(y, \pm L_3) + E_{45}W_{,y}(y, \pm L_3) + E_{55}U_{,3}(y, \pm L_3)\}^{(m)} = 0 \end{aligned} \quad \text{... (5)}$$

where, the subscript (*m*) denotes the outer-most layer.

A section perpendicular to the *z*-axis at the top of the k[th] layer is analyzed, where one-quarter of the laminate is considered. The free-body diagrams above and below this section, as viewed from the *x*-direction, are pictured in Figure 2. Equilibrium of forces in the *y*-direction above the section requires that;

$$\int_{t_k}^{L_3} \sigma_y(0,z)dz = \int_0^L \tau_{yz}^{(k)}(y,t_k)dy \quad (6)$$

$$\int_{t_k}^{L_3} \sigma_y(0,z)\, L_3(z - t_k)dz = \int_0^{L_2} \sigma_x^{(k)}(y,t_k)L_2 y dy \quad (7)$$

For the free-body diagram of quarter *x-z* plane with section at $t_k$, as shown in Figure 3, equilibrium of shear

forces in the *x*-direction requires that:

$$\int_0^{L_2} \tau_{xy}(y, t_k)\, dy = \int_0^{L_3} \tau_{xy}\,(0, z) dz \qquad \text{... (8)}$$

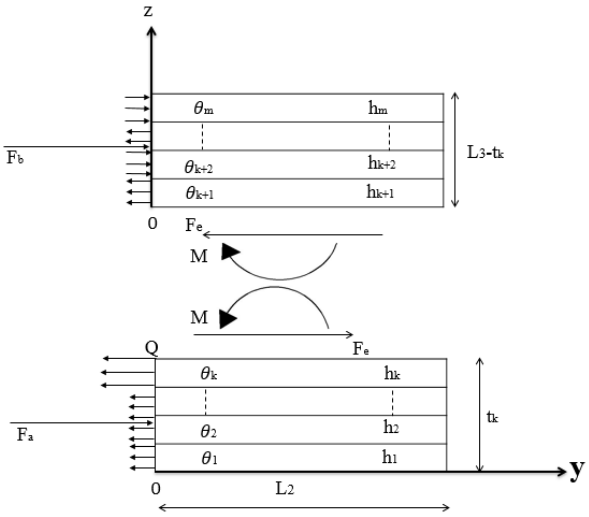


**Figure (2): Free-body diagram of quarter *y*-*z* plane with section at $t_k$ from *y*-axis**

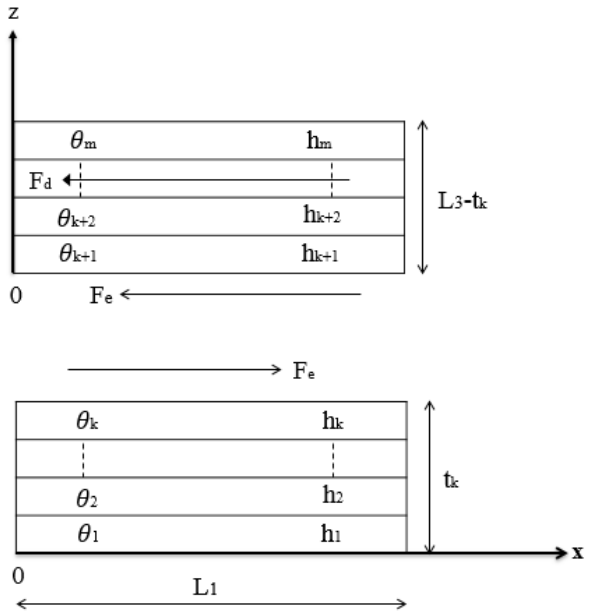


**Figure (3): Free-body diagram of quarter *x*-*z* plane with section at $t_k$ from *x*-axis**

**Finite Element Formulation**

Two types of isoperimetric elements are used; one in the interior region that has standard shape functions and the other in the boundary free-edge region that has a special kind of shape functions modeled from the zero-order perturbation solution of the boundary region. Shape functions are forced to satisfy the governing system of partial differential equations at the free-edge region according to the Galerkin approximation method. A three-dimensional eight-node linear isoperimetric element is used, since the laminate has linear edges in all directions. The same points, which are the corner nodes, are used to define the geometry and the other functions needed for the finite element analysis. As shown in Figure 4, a point within the isoperimetric element has the following coordinates:

$$X = \sum_{i=1}^{n} \psi_i X^{(i)}$$
$$Y = \sum_{i=1}^{n} \psi_i Y^{(i)} \qquad \text{... (9)}$$
$$Z = \sum_{i=1}^{n} \psi_i Z^{(i)}$$

where $X^{(i)}$, $Y^{(i)}$ and $Z^{(i)}$, for $i$=1,2,3,…,n are the coordinates for the $i^{th}$ node and $\psi_i$ for $i$=1,2,3,…,n is the standard three-dimensional shape function corresponding to the $i^{th}$ node.

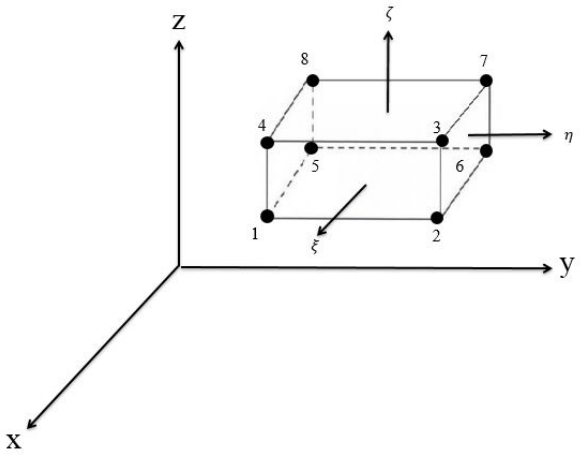


**Figure (4): Three-dimensional mapping of 3-D isoperimetric linear element**

**Three-dimensional Interior Region Shape Functions**

The isoperimetric element shown in Figure 4 has the following eight shape functions corresponding to the eight corner nodes.

$$\psi_i = \frac{1}{8}(1 + \xi i\xi)(1 + \eta_i\eta)(1 + \zeta_i\zeta) \qquad \text{... (10)}$$

where,

$\xi i = 1,1,1,1,-1,-1,-1,-1$
$\eta_i = -1,1,1,-1,-1,1,1,-1$
$\zeta_i = -1,-1,1,1,-1,-1,1,1$

for

$i = 1,2,3,4,5,6,7$ and $8$ and $\xi, \eta$ and $\zeta$ are the element local coordinates. These shape functions must satisfy the rigid-body mode,

$$\sum_{i=1}^{n} \psi_{i,} = 1 \quad \text{... (11)}$$

and $\psi_i$ has the value of one at the $i^{\text{th}}$ node and zero at the other nodes. These shape functions are convenient for the interior region, since the displacement functions vary smoothly.

**Three-dimensional Boundary Region Shape Functions**

For 3-D boundary element, the eight shape functions corresponding to the corner nodes are of the following form:

$$\begin{aligned} \mu_{1i} &= \alpha_1\psi_i + (1-\alpha_1)\phi_{1,i} \\ \mu_{2i} &= \alpha_2\psi_i + (1-\alpha_2)\phi_{2,i} \\ \mu_{3i} &= \alpha_3\psi_i + (1-\alpha_3)\phi_{3,i} \end{aligned} \quad \text{... (12)}$$

where $\mu_{1i}, \mu_{2i}$ and $\mu_{3i}$ correspond to the displacements in the $\xi, \eta$ and $\zeta$ directions, respectively and $\phi_{1,i}, \phi_{2,i}$ and $\phi_{3,i}$ take exponential forms in the $\eta$ −direction. Note that $0 \le \alpha_j \le 1$ (j=1,2,3) are smoothing parameters which make smooth transfer from the interior region to the boundary region. The shape functions which are defined in Equations (13) are simply the standard shape functions for $\alpha_j = 1$. The shape functions that define *u, v* and *w* for i = 1,2 and 3 respectively, are:

$$\begin{aligned}
\mu_{i1} &= \alpha_i[\frac{1}{8}(1+\xi)(1-\eta)(1-\zeta)] + (1-\alpha_i)[\frac{1}{4}\{1-\frac{1}{2}(1+\eta)(q_{i1}e^{\lambda_1(1-\eta)/e} \\
&\quad + q_{i2}e^{\lambda_2(1-\eta)/e} + q_{i3}e^{\lambda_3(1-\eta)/e})\}(1+\xi)(1-\zeta)] \\
\mu_{i2} &= \alpha_i[\frac{1}{8}(1+\xi)(1+\eta)(1-\zeta)] + (1-\alpha_i)[\frac{1}{8}(1+\eta)(q_{i1}e^{\lambda_1(1-\eta)/e} \\
&\quad + q_{i2}e^{\lambda_2(1-\eta)/e} + q_{i3}e^{\lambda_3(1-\eta)/e})(1+\xi)(1-\zeta)] \\
\mu_{i3} &= \alpha_i[\frac{1}{8}(1+\xi)(1+\eta)(1+\zeta)] + (1-\alpha_i)[\frac{1}{8}(1+\eta)(q_{i1}e^{\lambda_1(1-\eta)/e} \\
&\quad + q_{i2}e^{\lambda_2(1-\eta)/e} + q_{i3}e^{\lambda_3(1-\eta)/e})(1+\xi)(1+\zeta)] \\
\mu_{i4} &= \alpha_i[\frac{1}{8}(1+\xi)(1-\eta)(1+\zeta)] + (1-\alpha_i)[\frac{1}{4}\{1-\frac{1}{2}(1+\eta)(q_{i1}e^{\lambda_1(1-\eta)/e} \\
&\quad + q_{i2}e^{\lambda_2(1-\eta)/e} + q_{i3}e^{\lambda_3(1-\eta)/e})\}(1+\xi)(1+\zeta)] \\
\mu_{i5} &= \alpha_i[\frac{1}{8}(1-\xi)(1-\eta)(1-\zeta)] + (1-\alpha_i)[\frac{1}{4}\{1-\frac{1}{2}(1+\eta)(q_{i1}e^{\lambda_1(1-\eta)/e} \\
&\quad + q_{i2}e^{\lambda_2(1-\eta)/e} + q_{i3}e^{\lambda_3(1-\eta)/e})\}(1-\xi)(1-\zeta)] \\
\mu_{i6} &= \alpha_i[\frac{1}{8}(1-\xi)(1+\eta)(1-\zeta)] + (1-\alpha_i)[\frac{1}{8}(1+\eta)(q_{i1}e^{\lambda_1(1-\eta)/e} \\
&\quad + q_{i2}e^{\lambda_2(1-\eta)/e} + q_{i3}e^{\lambda_3(1-\eta)/e})(1-\xi)(1-\zeta)] \\
\mu_{i7} &= \alpha_i[\frac{1}{8}(1-\xi)(1+\eta)(1+\zeta)] + (1-\alpha_i)[\frac{1}{8}(1+\eta)(q_{i1}e^{\lambda_1(1-\eta)/e} \\
&\quad + q_{i2}e^{\lambda_2(1-\eta)/e} + q_{i3}e^{\lambda_3(1-\eta)/e})(1-\xi)(1+\zeta)] \\
\mu_{i8} &= \alpha_i[\frac{1}{8}(1-\xi)(1-\eta)(1+\zeta)] + (1-\alpha_i)[\frac{1}{4}\{1-\frac{1}{2}(1+\eta)(q_{i1}e^{\lambda_1(1-\eta)/e} \\
&\quad + q_{i2}e^{\lambda_2(1-\eta)/e} + q_{i3}e^{\lambda_3(1-\eta)/e})\}(1-\xi)(1+\zeta)]
\end{aligned} \quad \text{... (13)}$$

where, $\lambda_1$, $\lambda_2$ and $\lambda_3$ are the negative eigenvalues of the approximate solution. There are nine algebraic linearly independent equations; three of these nine equations are found using the fact that the shape functions must satisfy the rigid-body mode:

$$\begin{aligned} \sum_{i=1}^{8} \mu_{1i} &= 1 \\ \sum_{i=1}^{8} \mu_{2i} &= 1 \\ \sum_{i=1}^{8} \mu_{3i} &= 1 \end{aligned} \quad \text{... (14)}$$

The other six equations are found by making the shape functions corresponding to the boundary nodes, approximately satisfying the governing system of partial differential equations at the free-edge boundary. This could be done using the weighted residual approximation, such as the Galerkin method. Since there are twelve unknowns and nine linearly independent equations, $\alpha_j$ , $j = 1,2,3$ are specified and the following three sets of 3 equations and 3 unknowns, Equations (15), are solved for $q_{ij}$, $i = 1,2,3$ in terms of the smoothing parameters $\alpha_1, \alpha_2$ and $\alpha_3$ and the eigenvalues $\lambda_1$ , $\lambda_2$ and $\lambda_3$.

$$
\begin{aligned}
&q_{i1} + q_{i2} + q_{i3} = 1 \\
&\left(\frac{\lambda_1}{\epsilon}\right) q_{i1} + \left(\frac{\lambda_2}{\epsilon}\right) q_{i2} + \left(\frac{\lambda_3}{\epsilon}\right) q_{i3} = \frac{1}{2} + \frac{\alpha_i}{2(1 - \alpha_i)} \\
&\left\{\left(\frac{\lambda_1}{\epsilon}\right)^2 - \left(\frac{\lambda_1}{\epsilon}\right)\right\} q_{i1} + \left\{\left(\frac{\lambda_2}{\epsilon}\right)^2 - \left(\frac{\lambda_2}{\epsilon}\right)\right\} q_{i2} + \left(\frac{\lambda_3}{\epsilon}\right)^2 - \left(\frac{\lambda_3}{\epsilon}\right)\} q_{i3} = 0
\end{aligned}
\qquad \text{... (15)}
$$

**Three-dimensional Isoperimetric Linear Finite Element**

The point $p$ within the rectangular hexahedral element shown in Figure 2 has the following global coordinates in terms of the local coordinates:

$$
\begin{aligned}
x &= x_e + \frac{H_\xi}{2}\xi \\
y &= y_e + \frac{H_\eta}{2}\eta \\
z &= z_e + \frac{H_\zeta}{2}\zeta
\end{aligned}
\qquad \text{... (16)}
$$

where, $x_e, y_e$ and $z_e$ are the global coordinates of the centroid of the element and $H_\xi, H_\eta$ and $H_\zeta$ are the dimensions of the element in the $\xi, \eta$ and $\zeta$ directions, respectively. The displacements of point $p$ are given in terms of the eight corner nodes as follows:

$$
\begin{aligned}
u &= \sum_{i=1}^{8} N_{1i} u_i \\
v &= \sum_{i=1}^{8} N_{2i} v_i \\
w &= \sum_{i=1}^{8} N_{3i} w_i
\end{aligned}
\qquad \text{... (17)}
$$

where, $N_{1i} = \psi_{1i}$, $N_{2i} = \psi_{2i}$, $N_{3i} = \psi_{3i}$ for the interior region elements and $N_{1i} = \mu_{1i}$, $N_{2i} = \mu_{2i}$, $N_{3i} = \mu_{3i}$ , i = 1, 2, …8 for the boundary elements. Equation (17) could be written in a matrix form;

$$
\begin{Bmatrix} u \\ v \\ w \end{Bmatrix} = [N]\{d\} \qquad \text{... (18)}
$$

where,

$$
[N] = \begin{bmatrix}
N_{11} & 0 & 0 & N_{12} & 0 & 0 & \dots & \dots & \dots & N_{18} & 0 & 0 \\
0 & N_{21} & 0 & 0 & N_{22} & 0 & \dots & \dots & \dots & 0 & N_{28} & 0 \\
0 & 0 & N_{31} & 0 & 0 & N_{32} & \dots & \dots & \dots & 0 & 0 & N_{38}
\end{bmatrix}
$$

and

$$\{d\} = [u_1\ v_1\ w_1\ u_2\ v_2\ w_2 \dots \dots \dots\ u_s\ v_s\ w_s]^T$$

Minimization of total potential energy yields the following displacement equilibrium equations:

$$[K]\{d\} = \{R\} \qquad \text{... (19)}$$

where,

$$
\{R\} = -\int_{-1}^{1}\int_{-1}^{1}\int_{-1}^{1} \epsilon_0 [B]^T \begin{Bmatrix} E_{12} \\ E_{13} \\ 0 \\ 0 \\ E_{16} \end{Bmatrix} d\xi d\eta d\zeta \qquad \text{... (20)}
$$

is the stiffness matrix and

$$
\{R\} = -\int_{-1}^{1}\int_{-1}^{1}\int_{-1}^{1} \epsilon_0 [B]^T \begin{Bmatrix} E_{12} \\ E_{13} \\ 0 \\ 0 \\ E_{16} \end{Bmatrix} d\xi d\eta d\zeta \qquad \text{.. (21)}
$$

is the nodal forces due to the constant axial strain $\epsilon_0$ in the x-direction. The reduced elasticity matrix after substituting for $\epsilon_0$ is:

$$
[E_T] = \begin{bmatrix}
E_{22} & E_{23} & 0 & 0 & E_{26} \\
E_{13} & E_{23} & 0 & 0 & E_{36} \\
0 & 0 & E_{44} & E_{45} & 0 \\
0 & 0 & E_{45} & E_{55} & 0 \\
E_{26} & E_{36} & 0 & 0 & E_{66}
\end{bmatrix} \qquad \text{... (22)}
$$

$$[B] = [H][\Gamma][N'] \qquad \text{…(23)}$$

$$[H] = \begin{bmatrix} 0&0&0&0&1&0&0&0&0 \\ 0&0&0&0&0&0&0&0&1 \\ 0&0&0&0&0&1&0&1&0 \\ 0&0&1&0&0&0&1&0&0 \\ 0&1&0&1&0&0&0&0&0 \end{bmatrix} \quad \ldots(24)$$

$$[N'] = \begin{bmatrix} N_{11,\xi} & 0 & 0 & N_{12,\xi} & 0 & 0 & \ldots & \ldots & \ldots & N_{18,\xi} & 0 & 0 \\ N_{11,\xi} & 0 & 0 & N_{12,\xi} & 0 & 0 & \ldots & \ldots & \ldots & N_{18,\xi} & 0 & 0 \\ N_{11,\eta} & 0 & 0 & N_{12,\eta} & 0 & 0 & \ldots & \ldots & \ldots & N_{18,\eta} & 0 & 0 \\ 0 & N_{21,\xi} & 0 & 0 & N_{22,\xi} & 0 & \ldots & \ldots & \ldots & 0 & N_{28,\xi} & 0 \\ 0 & N_{21,\eta} & 0 & 0 & N_{22,\eta} & 0 & \ldots & \ldots & \ldots & 0 & N_{28,\eta} & 0 \\ 0 & N_{21,\zeta} & 0 & 0 & N_{22,\zeta} & 0 & \ldots & \ldots & \ldots & 0 & N_{28,\zeta} & 0 \\ 0 & 0 & N_{31,\xi} & 0 & 0 & N_{32,\xi} & \ldots & \ldots & \ldots & 0 & 0 & N_{38,\xi} \\ 0 & 0 & N_{31,\eta} & 0 & 0 & N_{32,\eta} & \ldots & \ldots & \ldots & 0 & 0 & N_{38,\eta} \\ 0 & 0 & N_{31,\zeta} & 0 & 0 & N_{32,\zeta} & \ldots & \ldots & \ldots & 0 & 0 & N_{38,\zeta} \end{bmatrix} \quad \ldots(25)$$

and $[\Gamma] = [\frac{2}{H_\xi}\ \frac{2}{H_\eta}\ \frac{2}{H_\zeta}\ \frac{2}{H_\xi}\ \frac{2}{H_\eta}\ \frac{2}{H_\zeta}\ \frac{2}{H_\xi}\ \frac{2}{H_\eta}\ \frac{2}{H_\zeta}]$ is 9x9 diagonal matrix.

Two Gauss-quadrature points in each direction are used when calculating the stiffness matrix and load vector for interior-region elements. This yields a good accuracy, since the derivatives of the shape functions vary smoothly in this region. However, due to the exponential growth or decay of the boundary elements' shape functions and their derivatives, integration using these quadrature points will ignore the boundary region, therefore leading to inaccurate estimation. For a boundary-region element, integration by parts is performed in the direction in which the shape functions vary exponentially and Gauss-quadrature numerical integration is used in the two other directions in which the shape functions vary smoothly. In other words, integration by parts is performed in the $\eta$ −direction and two-point Gauss-quadrature integration is used in each $\xi$ and $\zeta$ directions. The stiffness matrix [K] could be expanded as in the following form:

$$[K] = \sum_{i=0}^{15} [K_i] \quad \ldots (26)$$

where,

$$[K_0] = \int_{-1}^{1}\int_{-1}^{1}\int_{-1}^{1}[T_0]d\xi d\eta d\zeta \quad \ldots(27)$$

and the list of $[T_i]$ matrices is:

$$\begin{aligned}
&[T_0] = [N_0']^T[S][N_0'] \\
&[T_1] = [N_0']^T[S][N_1'] \\
&[T_2] = [N_0']^T[S][N_2'] \\
&[T_3] = [N_0']^T[S][N_3'] \\
&[T_4] = [N_1']^T[S][N_0'] \\
&[T_5] = [N_1']^T[S][N_1'] \\
&[T_6] = [N_1']^T[S][N_2'] \\
&[T_7] = [N_1']^T[S][N_3'] \\
&[T_8] = [N_2']^T[S][N_0'] \\
&[T_9] = [N_2']^T[S][N_1'] \\
&[T_{10}] = [N_2']^T[S][N_2'] \\
&[T_{11}] = [N_2']^T[S][N_3'] \\
&[T_{12}] = [N_3']^T[S][N_0'] \\
&[T_{13}] = [N_3']^T[S][N_1'] \\
&[T_{14}] = [N_3']^T[S][N_2'] \\
&[T_{15}] = [N_3']^T[S][N_3']
\end{aligned} \quad \ldots (28)$$

where, $[S] = [\Gamma]^T[\mathrm{H}]^T[ET][H][\mathrm{T}]$ and

$$\begin{aligned}
\Lambda_i = \lambda_1, \lambda_2, \lambda_3, \lambda_1, 2\lambda_1, \lambda_1 + \lambda_2, \lambda_1 + \lambda_3, \lambda_2, \lambda_1 \\
+ \lambda_2, 2\lambda_2, \lambda_2 + \lambda_3, \lambda_3, \lambda_1 + \lambda_3, \lambda_2 \\
+ \lambda_3, 2\lambda_3.
\end{aligned}$$

$for\ i = 1, 2, 3, 4, 5, 6, 7, 8, 9, 10, 11, 12, 13, 14, 15$

and

$$\begin{aligned}
&[K_i] \\
&= \int_{-1}^{1}\int_{-1}^{1} -\{\frac{\epsilon}{\Lambda_i}T_i(\xi, 1, \zeta) \\
&+ (\frac{\epsilon}{\Lambda_i})^2 T_{i,\eta}(\xi, 1, \zeta) \\
&+ (\frac{\epsilon}{\Lambda_i})^3 T_{i,\eta,\eta}(\xi, 1, \zeta)\}d\xi d\zeta
\end{aligned} \quad \ldots (29)$$

Similarly, the load vector of the boundary element could be expanded as follows:

$$\{R\} = -\sum_{i=0}^{3}\{R_i\} \quad \text{... (30)}$$

where,

$$\{R_0\} = \int_{-1}^{1}\int_{-1}^{1}\int_{-1}^{1}[f_0]d\xi d\eta d\zeta \quad \text{...(31)}$$

is integrated using two-point Gauss-quadrature integration in $\xi$ and $\zeta$ directions. After $\{R_i\}$ integration by parts in the n-direction and neglecting $e^{2\Lambda_i/\epsilon}$, the load vector reduces to the following 2-D integration:

$$\{R_i\} = -\int_{-1}^{1}\int_{-1}^{1}-\{\left(\frac{\epsilon}{\lambda_i}\right)f_i(\xi,1,\zeta) + (\frac{\epsilon}{\lambda_i})^2 f_{i,\eta}(\xi,1,\zeta)\}d\xi d\zeta \quad \text{... (32)}$$

for *i=1,2,3*

where,

$$\{f_i\} = \epsilon_0[N_i'][\Gamma]^T[\mathrm{H}]^T\begin{Bmatrix}E_{12}\\E_{13}\\0\\0\\E_{16}\end{Bmatrix} \quad \text{...(33)}$$

for *i=0,1,2,3.*

Equation (25) is integrated using two-point Gauss-quadrature in each of the $\xi$ and $\zeta$ directions.

## RESULTS AND DISCUSSION

High modulus graphite-epoxy material is used in this study. The properties of this material are: $E_x$ = *138 (GPa)*, $E_y = E_z$ = *4.5 (GPa)*, $G_{xy} = G_{xz} = G_{yz}$ = *5.86 (GPa)*, $v_{xy} = v_{zx} = v_{yz}$ = *0.21*, where *x,y* and *z* are the fiber, transverse and thickness directions, respectively. *E* is the modulus of elasticity; *G* is the shear modulus and *v* is the Poisson's ratio. Eigenvalues $\lambda_1, \lambda_2$ and $\lambda_3$ evaluated from the perturbation solution depend on material type and fiber orientation. Table 1 shows different values for $\lambda_1, \lambda_2$ *and* $\lambda_3$ for graphite-epoxy material and different fiber orientation angles, $\theta$, with respect to the *x*-axis. The composite laminates are symmetric; i.e., $\theta(z) = \theta(-z)$ with constant ply thickness $L_0$, constant width $2L_2$ and constant length $2L_1$. The plate is subjected to constant axial strain $\epsilon_x = \epsilon_0 = 1x10^{-6}$ m/m in the *x* direction. Different laminate sequences have been investigated. Cross-ply laminates with laminate sequences [0/90]s; i.e., [0/90/90/0] and [90/0]s; i.e., [90/0/0/90]. Angle-ply laminates with laminate sequences [0/0]s, [15/-15]s, [30/-30]s,[45/-45]s, [60/-60]s, [75/-75]s and [90/-90]s. Results obtained for different cases are compared with other solutions available in the literature for the same problem and loading condition. The effects of the geometric ratio and mesh refinement are also studied.

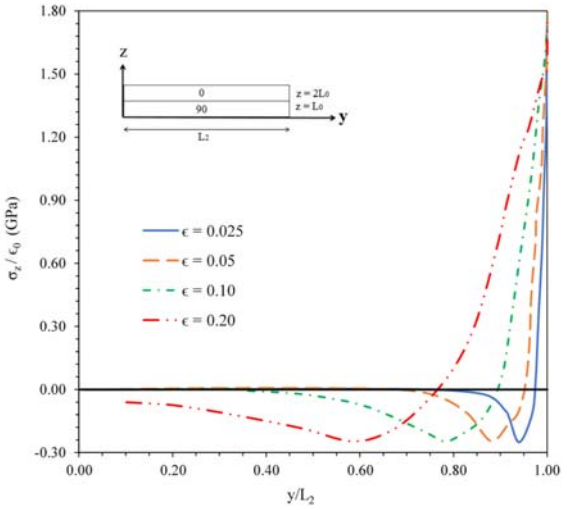


**Figure (5): Interlaminar normal stress, $\sigma_z$ at $z = 0$, distribution in the y-direction for different geometric ratios, $\epsilon$**

**Table 1. Different values for $\lambda_1, \lambda_2$ and $\lambda_3$ for graphite-epoxy material and different fiber orientations**

| $\theta$ Degrees | $\lambda_1$ | $\lambda_2$ | $\lambda_3$ |
|---|---|---|---|
| 0 | -1.100 | -1.000 | -0.902 |
| ± 15 | -1.126 | -0.907 | -0.637 |
| ± 30 | -1.159 | -0.937 | -0.392 |
| ± 45 | -1.209 | -0.966 | -0.380 |
| ± 60 | -1.364 | -0.987 | -0.241 |
| ± 75 | -1.507 | -0.997 | -0.218 |
| ± 90 | -1.576 | -1.000 | -0.210 |

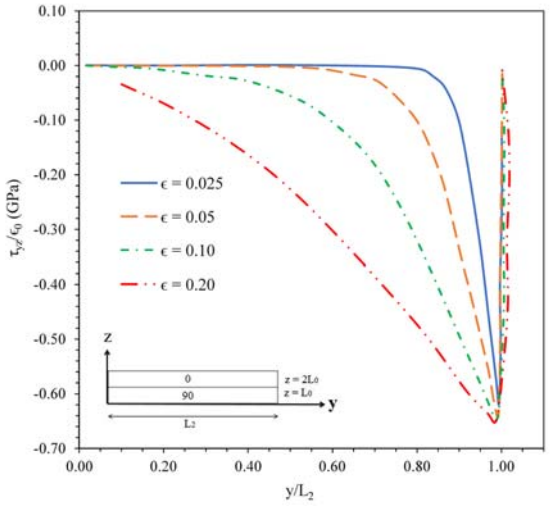


**Figure (6): Interlaminar shear stress, $\tau_{yz}$ at $z = 0$, distribution in y-direction for different geometric ratios, $\epsilon$**

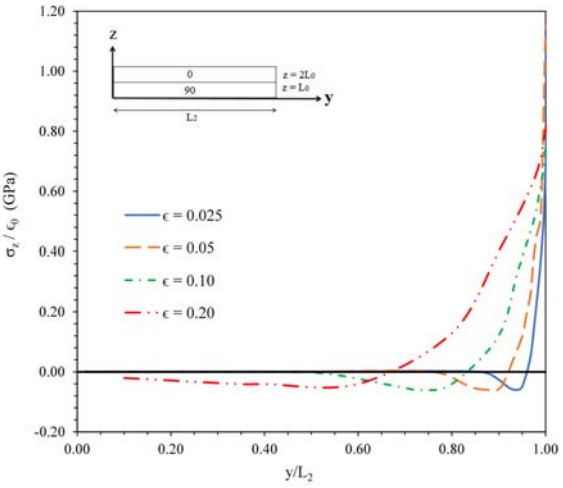


**Figure (7): Interlaminar normal stress, $\sigma_z$ at z = L0, distribution in the y-direction for different geometric ratios, $\epsilon$**

For cross-ply laminates oriented at either 0° or 90°, it should be noted that the interlaminar shear stress $\tau_{zx}$ is equal to zero, since there is no shear coupling. Interlaminar shear stress $\tau_{yz}$ and interlaminar normal stress $\sigma_z$ exist and have non-zero values, since there is a Poisson mismatch between the layers of the laminate. Interlaminar stresses $\sigma_z$ and $\tau_{yz}$ have a unique behavior in the boundary-layer region**.** Figures 5 through 7 show the distribution in the y-direction of interlaminar normal stress, $\sigma_z$ *and* interlaminar shear stress, $\tau_{yz}$, for different geometric ratios. The figures show that the boundary-layer region width decreases as the geometric ratio decreases. For a large ratio, $\epsilon$, the values of the interlaminar stresses $\sigma_z$ and $\tau_{yz}$ in the interior region are not equal to zero. This agrees with the assumptions of the classical lamination theory. The sharp change in the behavior of the interlaminar stresses $\sigma_z$ and $\tau_{yz}$ when approaching the boundary-layer region serves as a strong evidence of possible stress singularity in this region. The transverse displacement, *v* at $z = 2L_0$, as a function of *y* and for different geometric ratios is shown in Figure 8. The figure shows that the displacement variation is almost linear in the interior region and has an exponential growth in the boundary-layer region. The displacement distribution in the boundary-layer region becomes sharper as the geometric ratio becomes smaller. The value of the displacement increases as the value of the geometric ratio decreases. Figures 9 through 11 show the interlaminar normal stress distribution, $\sigma_z$, interlaminar shear stress distribution, $\tau_{yz}$ and transverse displacement distribution, *v*, for 50, 100, 160 and 240 three-dimensional, 24 degrees of freedom elements. For the evaluation of stresses, as shown in Figures 9 and 10, the 50-element mesh seems to be insufficient to get accurate results; however, the 100-element finer mesh serves the purpose as the 160- and 240-element meshes. For transverse displacement v, as shown in Figure 11, the 50-element mesh is almost as good as the 100-, 160- and 240-element meshes. Some of the obtained results are compared with the results available in the literature for the same problem and loading condition. Figures 12 through 15 provide a comparison of results obtained by the present model with other results obtained by Pagano (1978) and Wang & Crossman (1977), for geometric ratio, $\epsilon = \frac{1}{8}$. The results obtained by the present solution agree well with those obtained by other solutions, especially for the interlaminar normal stress distribution, $\sigma_z$, at $z = 0$ and the transverse displacement distribution, *v*, as shown in Figures 12 and 15. The finite-element solution by Wang & Crossman (1977) gives lower values of the normal stress at the exact free-edge and the peak shear stress. This is because their solution procedure is too dependent on the element's sizes in the free-edge region. A very refined mesh is needed to establish accurate results using the solution procedure in Wang and Crossman (1977). A uniform

mesh of 80 four-node rectangular elements is used to establish the results of the present solution. Wang and Crossman (1977) used a non-uniform mesh of 576 triangular elements to come up with their results which are shown in the same figures. This suggests that the present approach is superior to the FE procedure (Wang & Crossman, 1977) in saving computer storage and computing time. It is hard to establish an accurate solution using Pagano's theory (Pagano, 1978) or the method by Wang and Crossman (1977) for laminates consisting of many layers. The reason is that too many elements are needed, which yields unreasonable computer storage and computing time. Moreover, using the methods proposed by these authors will not yield satisfactory results for laminates with small geometric ratios. However, the present method is applicable for laminates consisting of many layers and produces accurate results for laminates with small geometric ratios, because only a few elements are needed for each layer. On the other hand, the present solution is being compared with solutions obtained by the perturbation method (Hsu & Herakovich, 1977; Wang & Dickson, 1978; Numayr, 1987). As shown in Figure 14, the results of different solution procedures are more pronounced in the boundary region in two aspects; the peak value of stress, where the present solution is 25% higher than the other solutions and the boundary width, where the present solution is about 50% less (0.1 compared to 0.2). These major differences between the different solutions are due to the fact that the present solution uses a special exponential FE shape that is capable of detecting exponential growth and decay in a narrow boundary region, while other solutions fail to do so.

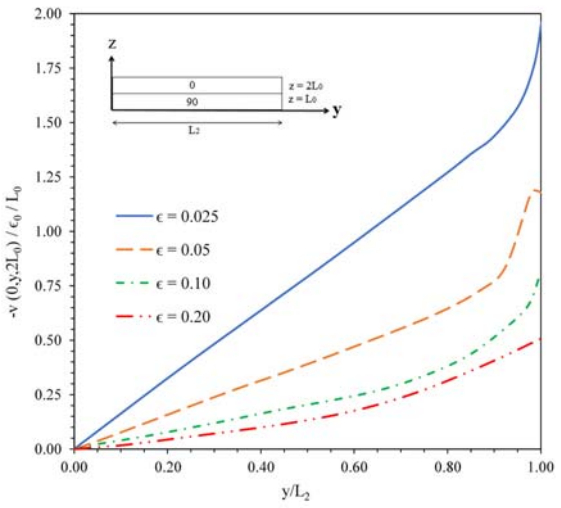


**Figure (8): Transverse displacement, v at the top free surface z = 2L0, variation in y-direction for different geometric ratios, $\epsilon$**

Figure 16 shows the interlaminar normal stress, $\sigma_z$ at $z = 0$ distribution in the y-direction for a small geometric ratio of 0.025. As shown in Figure 16, the perturbation solution (Hsu & Herakovich, 1977) yields a very small boundary layer width and a low normal stress value at the free edge. The reason is that the accuracy of the perturbation solution depends mainly on the geometric ratio and the relative values of material constants. It should be noted here that the distribution of normal stress is established using the $90^0$ layer as a reference layer. The perturbation solution (Hsu & Herakovich, 1977) is not expected to give a good accuracy when using the $90^0$ layer as a reference layer. This is due to the relative values of material constants. The coupled governing system of partial differential equations for bidirectional laminates is:

$$\begin{aligned}&(\frac{L_3}{L_2})^2E_{22}\Delta_{2,22}+\ E_{44}\Delta_{2,33}+\left(\frac{L_3}{L_2}\right)(E_{44}+E_{23})\Delta_{3,23}=0\\&(\frac{L_3}{L_2})(E_{44}+E_{23})\Delta_{2,23}+\ (\frac{L_3}{L_2})^2E_{44}\Delta_{3,22}+E_{33}\Delta_{3,33}=0\end{aligned} \quad \dots (34)$$

which for $L_2/L_3 = 0.05$ becomes:

$$(0^0)\begin{cases}0.0065\Delta_{2,22}\ +\Delta_{2,33}+0.0782\ \Delta_{3,23}=0\\ 0.030\Delta_{2,23}\ +0.001\ \Delta_{3,22}+\Delta_{3,33}=0\end{cases} \quad \dots (35)$$

$$(90^0)\begin{cases}0.05\Delta_{2,22}\ +\Delta_{2,33}+0.083\ \Delta_{3,23}=0\\0.032\Delta_{2,23}\ +0.001\ \Delta_{3,22}+\Delta_{3,33}=0\end{cases} \quad \dots (36)$$

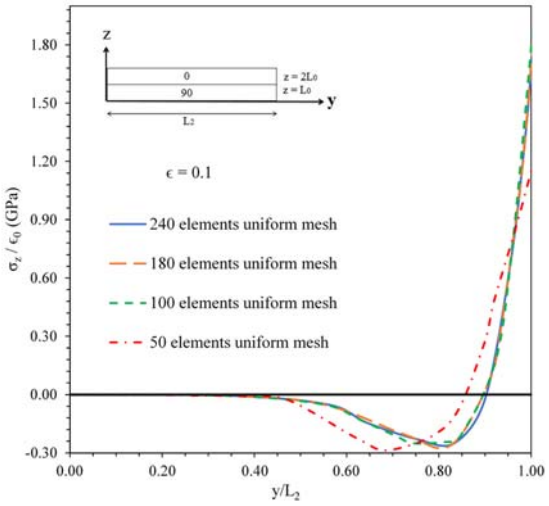


**Figure (9): Interlaminar normal stress, $\sigma_z$ at $z = 0$, distribution in the y-direction for different mesh sizes**

It can be observed from Equations (35) and (36) that a perturbation solution using the 0º layer as a reference layer should lead to more accurate results. Moreover, the zero-order perturbation solution is improved by diminishing $\epsilon$. The results for [90,0]s stacking sequence show that the signs of the interlaminar stresses are reversed, as expected by other solutions available in the literature.

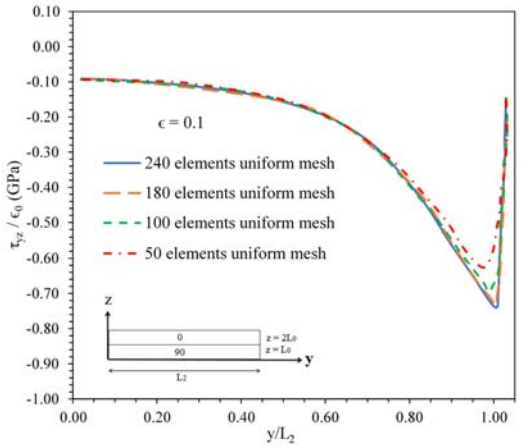


**Figure (10): Interlaminar shear stress, $\tau_{yz}$ at z = 0, distribution in y-direction for different mesh sizes**

All solutions follow the same trend of interlaminar normal stress distribution in the interior region that reverses to tensile stress in the boundary region in order to satisfy equilibrium in the z-direction. The present solution follows a smoother distribution due to the fact that it is a three-dimensional analysis and is in the $90^0$, $90^0$ interface with no sudden variation in the material properties. Also, since the laminates are relatively thick, a smoother variation is expected. The perturbation solution is so sensitive to $\epsilon$ which is relatively high; therefore, an accurate solution is not expected. On the other hand, the finite difference solution depends on the number of elements used; therefore, an accurate solution is not expected, since few elements are used. At the exact free edge, there is a high variation in normal stress value and the present solution yields approximately the average of other solutions.

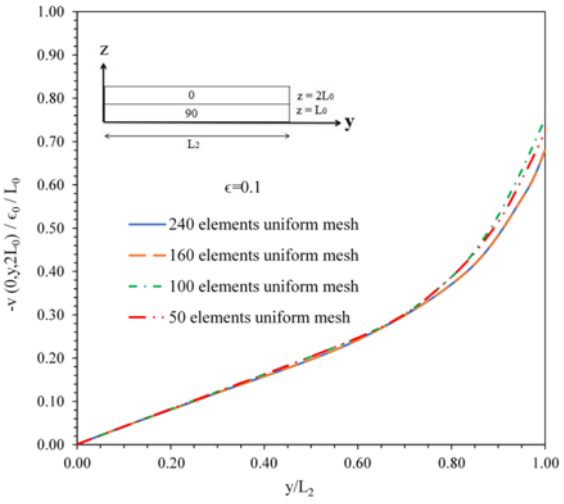


**Figure (11): Transverse displacement, v at z = 2L0, variation in y-direction for different mesh sizes**

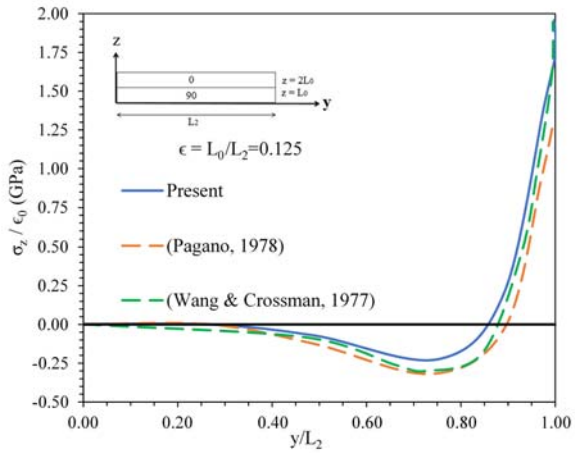


**Figure (12): Interlaminar normal stress, $\sigma_z$ at z = 0, distribution in y-direction for the present, (Pagano, 1978) and (Wang & Crossman, 1977) solutions**

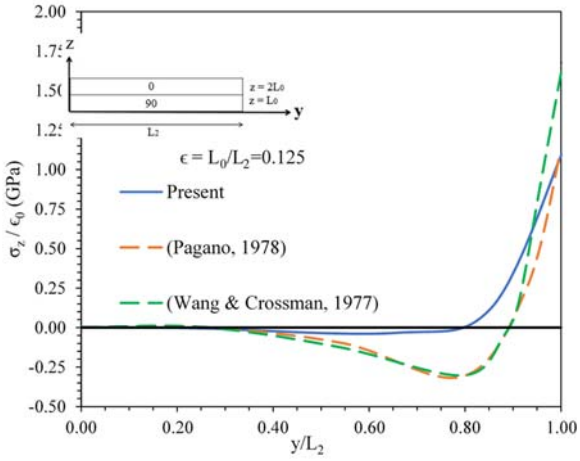


**Figure (13): Interlaminar normal stress, $\sigma_z$ at z = L₀ , distribution in y-direction for the present, (Pagano, 1978) solutions**

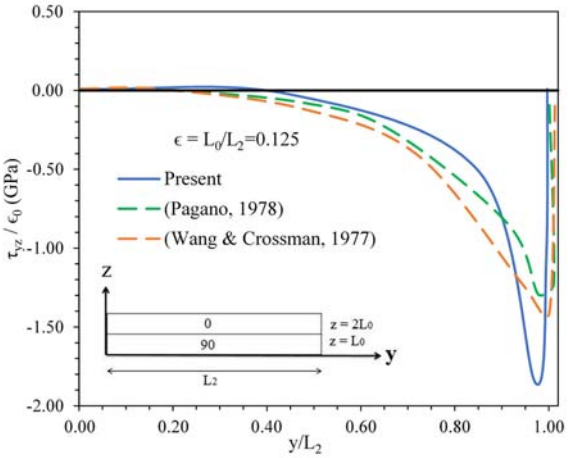


**Figure (14): Interlaminar shear stress, $\tau_{yz}$ at z = Lo, distribution in y-direction for the present, (Pagano, 1978) and (Wang & Crossman, 1977) solutions**

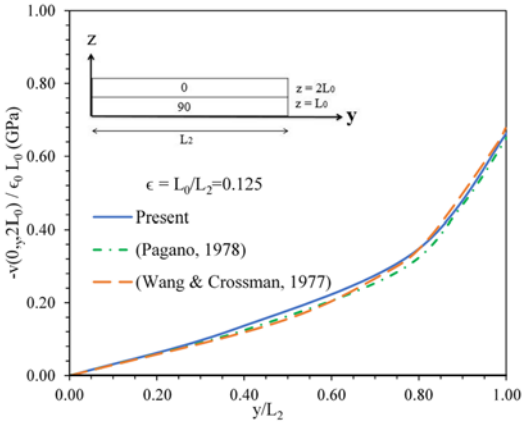


**Figure (15): Transverse displacement, *v* at the top free surface *z = 2L₀*, for the present, (Pagano, 1978) and (Wang & Crossman, 1977) solutions**

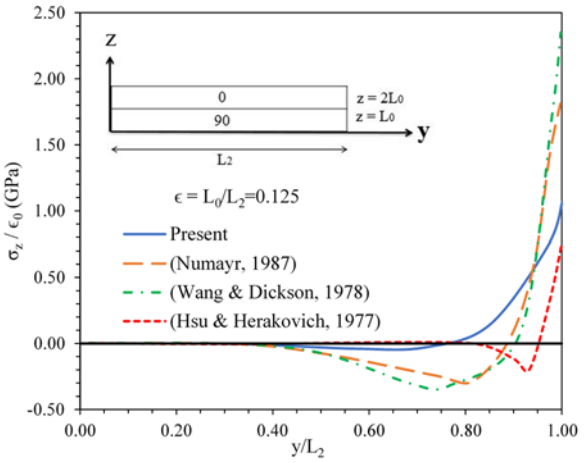


**Figure (16): Interlaminar normal stress, $\sigma_z$ at *z = 0,* distribution in y-direction for present, (Numayr, 1987), (Wang & Dickson, 1978) and (Hsu & Herakovich, 1977) solutions, $\epsilon$ = 0.025**

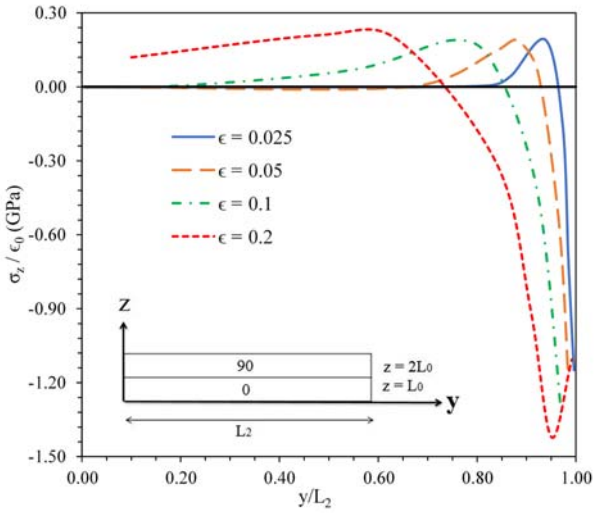


**Figure (17): Interlaminar normal stress, $\sigma_z$ at $z = 0$, distribution in *y*-direction for different geometric ratios, $\epsilon$**

Figure 17 shows the distribution in the y-direction of interlaminar normal stress, $\sigma_z$ at $z = 0$, for different geometric ratios. The figure shows that the width of the boundary-layer region decreases as the geometric ratio decreases. The value of the interlaminar stresses in the interior region converges to zero as the value of the geometric ratio becomes smaller. This is in good agreement with classical lamination theory. The sharp variation in the behavior of the interlaminar normal stress, $\sigma_z$ , as approaching the free edge, is an indication of possible stress singularity at that region. As expected, it can be noticed that the normal stress distribution at mid-plane 00 and 00 interlaminar layer is opposite to

that at 90 and 900 interlaminar layer. Tensile stress peak value in the interior region and compressive stress peak value are not much affected by ϵ, since the interlaminar stresses are evaluated at 00 and 00 interface layer with no sudden change in material properties. The main effect of ϵ is that the peak tensile stress is shifted toward the free-edge as ϵ decreases.

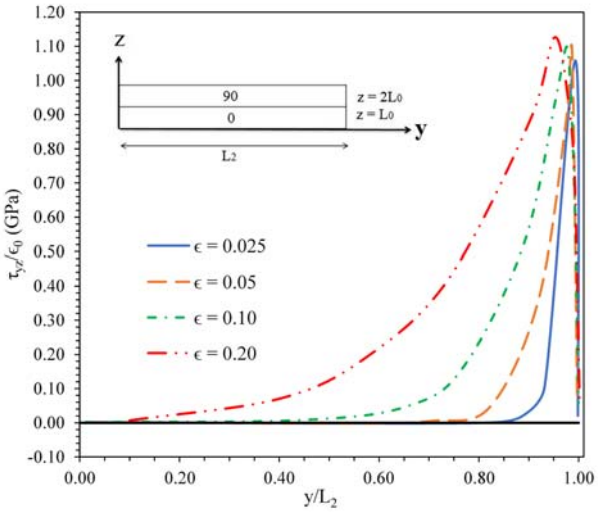


**Figure (18): Interlaminar shear stress, $\tau_{yz}$ at $z = 0$, distribution in y-direction for different geometric ratios, $\epsilon$**

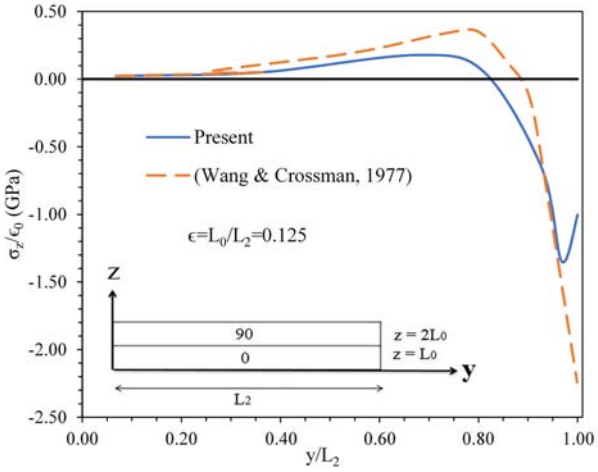


**Figure (19): Interlaminar normal stress, $\sigma_z$, at z = 0, distribution in y-direction for present and (Wang & Crossman, 1977) solutions for geometric ratio, $\epsilon$ = 0.125**

Figure 18 shows the interlaminar shear stress distribution in the y direction, $\tau_{yz}$ at $z = 0$, for different geometric ratios. This figure also shows that the width of the boundary-layer region decreases as the value of geometric ratio decreases. A comparison between the present solution and the solution obtained by Wang and Crossman (1977), for the interlaminar normal stress distribution in the $y$ direction for geometric ratio $\epsilon$ = 0.125, is shown in Figure 19. Even though $\sigma_3$ from both solutions converge to almost the same finite negative maximum value at the free edge, the present solution provides a smaller boundary-layer width and a sharper rise in the magnitude of stress at the free edge. The present approach has an advantage over the other finite element approach by Wang and Crossman (1977), since a considerably less number of elements is needed to establish an accurate solution. For interlaminar normal stress distribution in the y-direction and a geometric ratio of 0.025, Figure 20 presents a comparison between the present solution and the solutions obtained by perturbation technique (Hsu & Herakovich, 1977; Numayr, 1987). The present solution exhibits better agreement with the perturbation solution (Hsu & Herakovich, 1977). The value of $\sigma_3$ at the exact free-edge and the value of maximum positive stress for both solution approaches are almost the same. The perturbation solution yields more accurate results when using the $0^0$ as a reference layer, as illustrated in Equations (35) and (36). Therefore, the present solution is more reliable when using the $90^0$ as a reference layer.

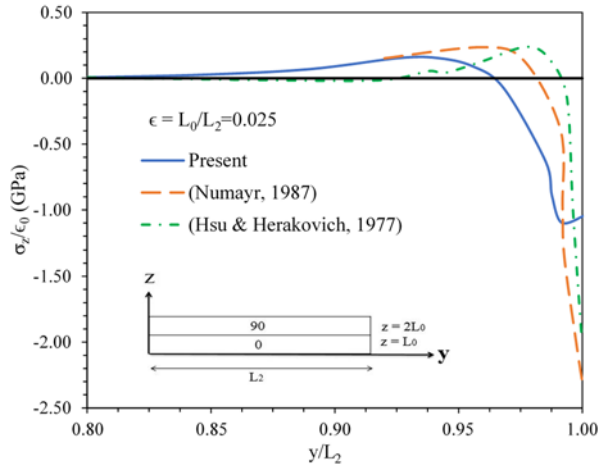


**Figure (20): Interlaminar normal stress, $\sigma_z$, at z = Lo, distribution in y-direction for present, (Numayr, 1987) and (Hsu & Herakovich, 1977), solutions geometric ratio, $\epsilon$ = 0.025**

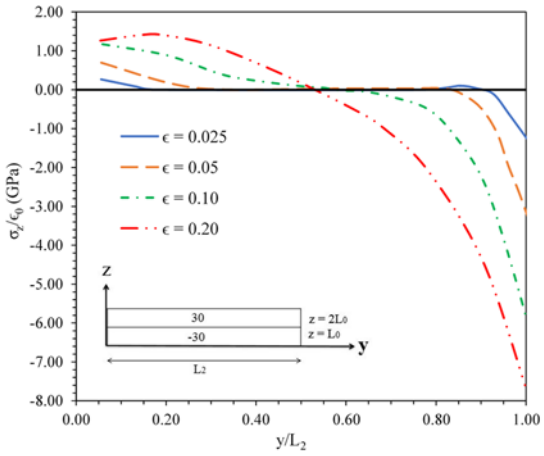


**Figure (21): Interlaminar normal stress, $\sigma_z$, at z = Lo, distribution in y-direction for [30/-30]s composite laminate and different geometric ratios, $\epsilon$**

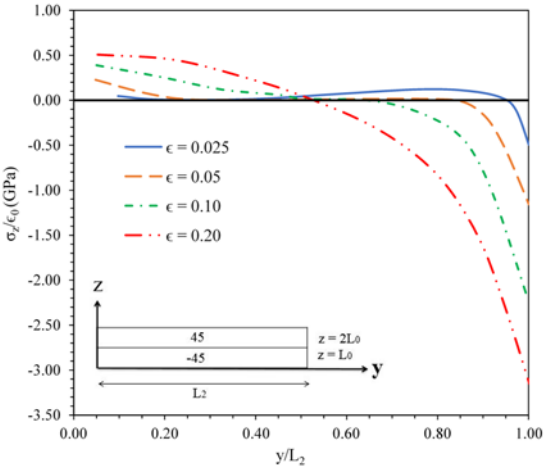


**Figure (22): Interlaminar normal stress, $\sigma_z$, at z = Lo, distribution in y-direction for [45/-45]s composite laminate and different geometric ratios, $\epsilon$**

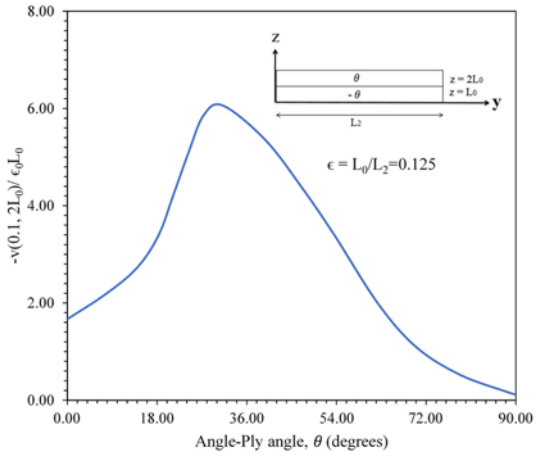


**Figure (23): Maximum transverse displacement at y = L2 and z = 2L0, for different angle-ply angles, $\theta$**

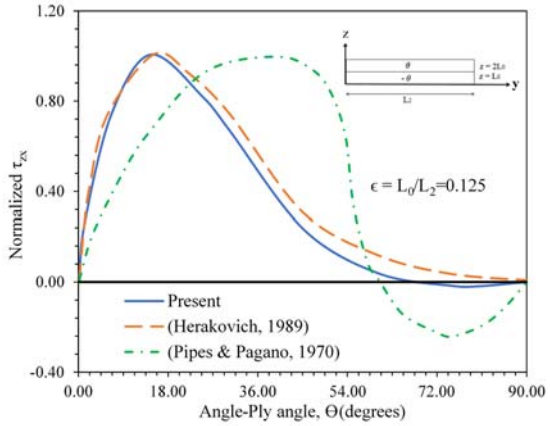


**Figure (24): Interlaminar shear stress, $\tau_{zx}$, for different angle-ply angles at geometric ratio, $\epsilon = 0.125$**

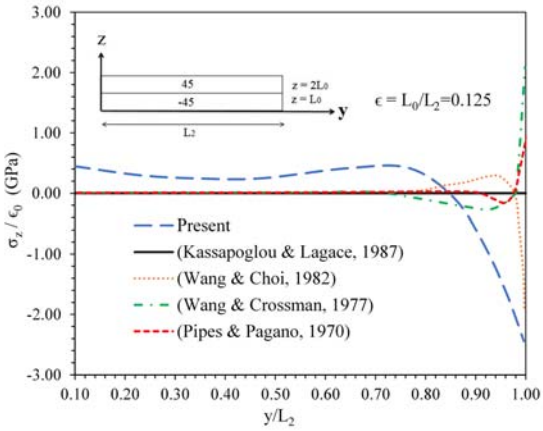


**Figure (25): Interlaminar normal stress, $\sigma_z$ at z = 0, distribution in y-direction for [45/-45]s angle-ply laminate and for different solutions**

Angle-ply laminates are composed of an equal number of layers with fibers oriented at $+\theta$ and $-\theta$. Due to shear coupling in angle-ply laminates, interlaminar stress, $\tau_{xz}$ , is important and should be determined. Figures 21 and 22 show the distribution in y direction of the interlaminar normal stress, $\sigma_z$ at $z = L_0$, for angle-ply laminates [30, -30]s and [45,-45]s. The figures show that the interlaminar normal stress, $\sigma_z$ , increases as the geometric ratio increases. The distribution of this stress in the interior region goes to zero as the geometric ratio becomes smaller. Hence, the finite element model agrees with the assumptions of classical lamination theory for thin laminates, where the theory yields satisfactory solutions. As shown in Figure 23, the maximum transverse displacement at the surface of top

free layer, $z = 2L_0$, which occurs at the free edge, $y = L_2$, is plotted for angle-ply laminates with angle range $\theta$ = 0° to 90°. It can be noticed that the maximum displacement occurs when the angle of the angle-ply laminate is 45°, while the minimum displacement occurs when the angle of the angle-ply laminate is 90°.

Figure 24 shows normalized interlaminar normal stress and interlaminar shear stress for a geometric ratio of 0.125. The figure shows that the maximum interlaminar stresses are most likely to occur at an angle, $\theta$ =15°, or lower. Figure 24 also provides comparisons between the results obtained by the present method and those obtained by Herakovich (1989) and Pipes and Pagano (1970). It is shown that the maximum interlaminar shear stress, $\tau_{xz}$ , occurs at an angle of 15°, for the present and Herakovich (1989) solutions, while it occurs at an angle of 35° for Pipes and Pagano (1970) solution. The distribution in the y-direction of interlaminar normal stress, $\sigma_z$ at $z = 0$, for an angle-ply laminate with angle $\theta$ = 45° and geometric ratio, $\epsilon$ =0.125, is shown in figure 25. This figure shows results of different solutions; the present, (Pipes & Pagano, 1970), (Wang & Crossman, 1977), (Wang & Choi, 1982) and (Kassapoglou & Lagace, 1987) solutions. As can be noticed, the present solution agrees well with the solution obtained by Wang & Choi (1982) in the boundary-layer region, but in the interior region, the solution does not converge to zero because of the use of a large value of geometric ratio, which is in good agreement with assumptions of the classical lamination theory.

## CONCLUSIONS

In this paper, a finite element model is proposed for modeling edge effects in composite laminates with different ply orientations. An original finite element computer program is used to solve the problem of symmetrical composite laminated plates subjected to constant axial strain with different laminate sequences, different geometric ratios and different mesh sizes. Results are obtained for cross-ply laminates [0/90]s and [90/0]s and angle-ply laminates with angles; + or – ( 0°, 15°, 30°, 45°, 60°, 75°, 90°). In cross-ply laminates, the interlaminar shear stress, $\tau_{zx}$, is zero, because there is no shear coupling and only the two interlaminar stresses $\sigma_z$ and $\tau_{yz}$ have non-zero values because of the Poisson mismatch. In angle-ply laminates, the three interlaminar stresses, $\sigma_z$, $\tau_{yz}$ and $\tau_{zx}$ have non-zero values because of the Poisson mismatch and shear coupling effects. In addition to material properties, geometric ratio is a main parameter in determining deformations and stresses, hence determining possible delamination and understanding the free-edge effect. The width of the boundary-layer region decreases as the geometric ratio decreases. The exponential growth or decay behavior of interlaminar stress distribution in a narrow boundary-layer region is an evidence on possible singularity in this region. Therefore, a high probability of delamination is expected as a result of the free-edge effects. The value of the interlaminar stress in the interior region converges to zero as the geometric ratio becomes smaller; hence, this behavior agrees with the assumptions of the classical lamination theory.

**Declaration of Competing Interest**

The authors declare that they have no known competing financial interests or personal relationships that could have appeared to influence the work reported in this paper.

This research did not receive any specific grant from funding agencies in the public, commercial or not-for-profit sectors.

## REFERENCES

Bar-Yoseph, P., and Avrashi, J. (1986). “New variational-asymptotic formulations for interlaminar stress analysis in laminated plates". Zeitschrift für angewandte Mathematik und Physik (ZAMP), 37 (3), 305-321. https://doi.org/10.1007/BF00946753

Cao, D., Hu, H., Duan, Q., Song, P., and Li, S. (2019). “Experimental and three-dimensional numerical investigation of matrix cracking and delamination interaction with edge effect of curved composite laminates”. Composite Structures, 225, 111154. https://doi.org/10.1016/J.COMPSTRUCT.2019.111154

Cater, C.R., Xiao, X., Goldberg, R.K., and Gong, X. (2018). "The influence of interlaminar microstructure on micro-cracking at laminate free edge". Composites-Part A: Applied Science and Manufacturing, 110, 217-226. https://doi.org/10.1016/J.COMPOSITESA.2018.04.007

Chorng-Fuh, L., and Horng-Shian, J. (1993). "A new finite-element formulation for interlaminar stress analysis". Computers & Structures, 48 (1), 135-139. https://doi.org/10.1016/0045-7949(93)90464-O

Dölling, S., Hahn, J., Felger, J., Bremm, S., and Becker, W. (2020). "A scaled boundary finite-element method model for interlaminar failure in composite laminates". Composite Structures, 241, 111865. https://doi.org/10.1016/J.COMPSTRUCT.2020.111865

Espadas-Escalante, J.J., van Dijk, N.P., and Isaksson, P. (2018). "The effect of free edges and layer shifting on intralaminar and interlaminar stresses in woven composites".Composite Structures, 185, 212-220. https://doi.org/10.1016/J.COMPSTRUCT.2017.11.014

Herakovich, C.T. (1989). "Edge effects and delamination failures". The Journal of Strain Analysis for Engineering Design, 24 (4), 245-252.

Herakovich, C.T., Post, D., Buczek, M.B., and Czarnek, R. (1985). "Free-edge strain concentrations in real composite laminates: Experimental-theoretical correlation". Journal of Applied Mechanics, 52 (4), 787-793. https://doi.org/10.1115/1.3169147

Hsu, P.W., and Herakovich, C.T. (1977). "Perturbation solution for interlaminar stresses in bidirectional laminates". ASTM Special Technical Publication, 617, 296-316. https://doi.org/10.1520/STP26950S

Islam, M.S., and Prabhakar, P. (2017). "Modeling framework for free-edge effects in laminates under thermo-mechanical loading". Composites-Part B: Engineering, 116, 89-98. https://doi.org/10.1016/J.COMPOSITESB.2017.01.072

Kassapoglou, C., and Lagace, P.A. (1987). "Closed-form solutions for the interlaminar stress field in angle-ply and cross-ply laminates". Journal of Composite Materials, 21 (4), 292-308.

Kumar, S., Kumar, R., and Mandal, S. (2020). "Finite-element analysis of composite hat-stiffened panels subjected to edge compression load". Jordan Journal of Civil Engineering, 14 (2).

Lecomte-Grosbras, P., Réthoré, J., Limodin, N., Witz, J.F., and Brieu, M. (2014). "Three-dimensional investigation of free-edge effects in laminate composites using X-ray tomography and digital volume correlation". Experimental Mechanics, 55 (1), 301-311. https://doi.org/10.1007/S11340-014-9891-1

Lorriot, T., Wargnier, H., Wahl, J.C., Proust, A., and Lagunegrand, L. (2013). "An experimental criterion to detect onset of delamination in real time". https://doi.org/10.1177/0021998313495069

Mohammadi, B., and Salimi-Majd, D. (2014). "Investigation of delamination and damage due to free-edge effects in composite laminates using cohesive interface elements". Engineering Solid Mechanics, 2 (2), 101-118.

Nguyen, V.T., and Caron, J.F. (2006). "A new finite element for free-edge effect analysis in laminated composites". Computers & Structures, 84 (22-23), 1538-1546. https://doi.org/10.1016/J.COMPSTRUC.2006.01.038

Nguyen, V.T., and Caron, J.F. (2009). "Finite-element analysis of free-edge stresses in composite laminates under mechanical and thermal loading". Composites Science and Technology, 69 (1), 40-49. https://doi.org/10.1016/J.COMPSCITECH.2007.10.055

Numayr, K.S. (1987). "Finite-element method for modeling edge effects in composite laminates". Univ. of Southern California, Los Angeles, CA.

Oplinger, D.W., Parker, B.S., and Chiang, F.P. (1974). "Edge-effect studies in fiber-reinforced laminates". Experimental Mechanics, 14 (9), 347-354. https://doi.org/10.1007/BF02323560

Pagano, N.J. (1978). "Stress fields in composite laminates". International Journal of Solids and Structures, 14 (5), 385-400. https://doi.org/10.1016/0020-7683(78)90020-3

Pereira, C.M.C., and Martins, M.S.S. (2014). "Flame retardancy of fiber-reinforced polymer composites based on nanoclays and carbon nanotubes". Polymer Green Flame Retardants, 551-595. https://doi.org/10.1016/ B978-0-444-53808-6.00017-2

Pipes, R.B., and Daniel, I.M. (2016). "Moiré analysis of the interlaminar shear-edge effect in laminated composites". https://doi.org/10.1177/002199837100500211

Pipes, R.B., and Pagano, N.J. (1970). "Interlaminar stresses in composite laminates under uniform axial extension".

Romera, J.M., Cantera, M.A., Adarraga, I., and Mujika, F. (2013). "Application of the sub-modeling technique to the analysis of the edge effects of composite laminates". https://doi.org/10.1177/0731684413482995

Shen, L., Liu, L., Zhou, Y., and Wu, Z. (2020). "Thickness effect of carbon nanotube interleaves on free-edge delamination and ultimate strength within a symmetric composite laminate". Composites-Part A: Applied Science and Manufacturing, 132, 105828. https://doi.org/10.1016/J.COMPOSITESA.2020.105828

Solis, A., Sánchez-Sáez, S., and Barbero, E. (2018). "Influence of ply orientation on free-edge effects in laminates subjected to in-plane loads". Composites-Part B: Engineering, 153, 149-158. https://doi.org/10.1016/J.COMPOSITESB.2018.07.030

Wang, A.S.D., and Crossman, F.W. (1977). "Some new results on edge effect in symmetric composite laminates". Journal of Composite Materials, 11 (1), 92-106.

Wang, J.T., and Dickson, J.N. (1978). "Interlaminar stresses in symmetric composite laminates". Journal of Composite Materials, 12 (4), 390-402.

Wang, S.S., and Choi, I. (1982). "Boundary-layer effects in composite laminates: Part 1-Free-edge stress singularities". Journal of Applied Mechanics, 49 (3), 541-548. https://doi.org/10.1115/1.3162514

Yang, D., Sheng, Y., Ye, J., and Tan, Y. (2011). "Dynamic simulation of crack initiation and propagation in cross-ply laminates by DEM". Composites Science and Technology, 71 (11), 1410-1418. https://doi.org/10.1016/J.COMPSCITECH.2011.05.014.